

# Mechanical performance and oxidation resistance of an ODS $\gamma$ -TiAl alloy processed by spark plasma sintering and laser additive manufacturing

C. Kenel<sup>1,2</sup>, A. Lis<sup>1,3</sup>, K. Dawson<sup>4</sup>, M. Stiefel<sup>1</sup>, C. Pecnik<sup>1</sup>, J. Barras<sup>5</sup>, A. Colella<sup>6</sup>, C. Hauser<sup>5</sup>, G.J. Tatlock<sup>4</sup>, C. Leinenbach<sup>1,\*</sup>, K. Wegener<sup>2</sup>

<sup>1</sup> Empa - Swiss Federal Laboratories for Materials Science and Technology, Überlandstrasse 129, 8600 Dübendorf, Switzerland

<sup>2</sup> ETH Zürich, IWF - Institute for Machine Tools and Manufacturing, Leonhardstrasse 21, Zurich, Switzerland

<sup>3</sup> Division of Materials and Manufacturing Science, Graduate School of Engineering, Osaka University, Suita, Japan

<sup>4</sup> Centre for Materials and Structures, School of Engineering, University of Liverpool, Brownlow Hill, Liverpool L69 3GH, UK

<sup>5</sup> TWI Technology Centre Yorkshire, Advanced Manufacturing Park, Wallis Way, Catcliffe Rotherham. S60 5TZ, UK

<sup>6</sup> MBN Nanomaterialia S.p.A., Via G. Bortolan 42, 31050 Vascon di Carbonera (TV), Italy

\* corresponding author: Christian.Leinenbach@empa.ch, Tel: +41 58 765 4518

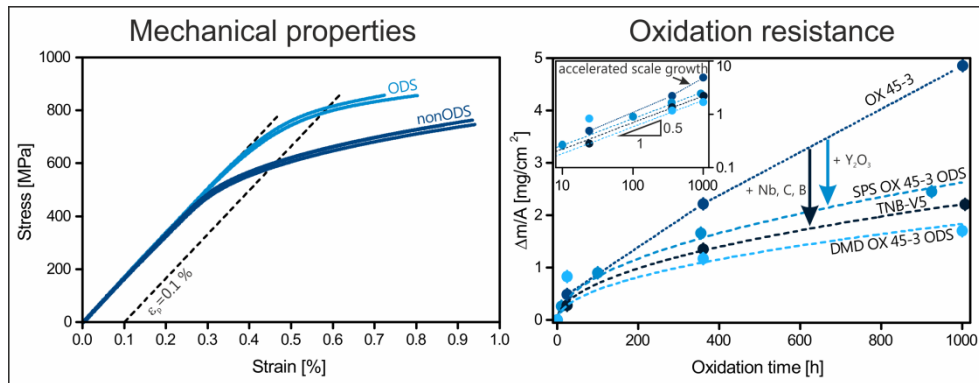
## Abstract

In this work, the influence of  $Y_2O_3$  additions on the mechanical properties and oxidation resistance of a Ti-45Al-3Nb (at.%) alloy have been studied. In particular, the mechanical properties from 293 K to 1073 K and oxidation resistance at 1073 K of spark plasma sintered and direct metal deposited material have been examined. At room temperature, higher yield stress (+34%) and ultimate tensile strength (+14%) at reduced ductility (-17%) is observed for the oxide dispersion strengthened variant compared to its non-strengthened counterpart. The strengthened variant shows superior strength retention up to 1073 K. Strengthened direct metal deposited material shows similar deformation characteristics as sintered material but suffers from premature fracture due to residual porosity. The addition of  $Y_2O_3$  increases the oxidation resistance of both sintered and direct metal deposited material. Parabolic growth constants are decreased by -49% and -75% in sintered and direct metal deposited material, respectively. In sintered material the dispersoid size shows only slight changes from 29 nm to 26 nm at 923 K after 987 h and to 32 nm at 1073 K after 924 h demonstrating the high stability of the added particles. TEM analysis reveals abundant grain boundary pinning by the particles contributing to microstructural stability. The results show the potential of oxide dispersion strengthening in titanium aluminides for conventional sintering as well as for additive manufacturing processing routes.

## Keywords

gamma-TiAl, oxide dispersion strengthened, additive manufacturing, spark plasma sintering, mechanical properties, oxidation resistance

## Graphical abstract



## 1 Introduction

Composite materials based on a TiAl matrix have been considered for high temperature applications since the development of the first TiAl alloys [1]. Regarding the coefficient of thermal expansion (CTE), the oxides  $\text{Al}_2\text{O}_3$ ,  $\text{Y}_2\text{O}_3$  and  $\text{ZrO}_2$  are similar to the TiAl matrix while SiC and  $\text{Si}_3\text{N}_4$  have significantly smaller CTEs [2]. Chemical compatibility with the matrix is essentially stability against the aggressive TiAl melt. Only a handful of materials is more stable than the reaction products of Ti and Al with O and N. Minimal reactivity is observed for rare earth oxides of group III of the periodic table of the elements and Al with the  $\text{M}_2\text{O}_3$  stoichiometry [3]. Additions of oxide particles to intermetallics have been proposed early on for the FeAl, NiAl and TiAl systems [5]. The oxide dispersion strengthened (ODS) systems NiAl and FeAl have been studied in detail using  $\text{Y}_2\text{O}_3$  as the dispersed phase [5,6]. ODS TiAl has theoretical advantages over ODS NiAl in terms of compatibility with the strengthening particles and a higher melting point of the matrix [3]. Early attempts using B and Er additions were published in 1991 by Schwartz et al. [10]. Suryanarayana and Froes [11] later reviewed the addition of Er and Gd to a  $(\alpha_2+\beta)$  Ti-25Al-10Nb-3V-1Mo alloy to form the corresponding oxides as fine particles. Uniform particle dispersion could not be obtained. However, the reported results indicated enhanced hardness without excessive embrittlement of the alloys. Later studies by Trivedi et al. [12] used Y additions in GE48-2-2 to form an ODS material by mechanical alloying and hipping. In the studied alloy the particles restricted grain growth up to 1423 K. These results indicate superior properties of ODS titanium aluminides compared to their non-strengthened parent alloy regarding low and high temperature strength without losses in fracture toughness and ductility. Recently, the fabrication of *in situ* TiAl/ $\text{Al}_2\text{O}_3$  composites was reported [13,14]. The resulting strengthening effects could be attributed to the presence of the oxide particles and the reduced grain size. Only a few studies have been published on ODS TiAl despite the potential to provide superior properties compared to established ODS intermetallics.

The beneficial effects upon addition of rare earth elements on oxidation resistance and the associated rare earth effect (REE) are well known and exploited in many state-of-the-art alloy systems, especially in Ni- and Fe-based alloys [15]. In alumina-forming alloys, the elements Y and Hf were found to be equally effective [16]. Later work, as reviewed by Pint [17], provided estimations for suitable addition levels and element combinations in alumina formers. The combination of Y with Hf or Zr provides the highest oxidation resistance, but as a single addition Y is more effective than the other elements. It was also observed that ideally Hf and Zr levels around 0.05 at.% are applied, while slightly higher Y contents in the range of 0.1 at.% provide the best results.

While the REE can increase oxidation resistance in alumina-forming alloys by more than one order of magnitude, its effect on marginal alumina-forming alloys is much lower. TiAl alloys and other aluminides are an example of such alloys, as they tend to form mixed scales consisting of  $\text{Al}_2\text{O}_3$  and

TiO<sub>2</sub> instead of the desired pure alumina scale [18]. For TiAl alloys, the effects of Y addition on the oxidation resistance have been classified as beneficial, neutral or even detrimental in the past. Taking into account the specifics of the REE, in the case of additions exceeding a 1 at.% over-doping leads to a similar or inferior oxidation resistance compared to the un-doped base alloy [17,18]. However for low Y levels in the alloy or applied as a coating, beneficial [19–24], detrimental and neutral effects have been described [20,21,25,26]. The beneficial effects refer to reduced scale growth rates and increased scale adherence, while the observed detrimental effects are internal oxidation of Y forming locally Y<sub>2</sub>O<sub>3</sub> or only limited protection due to Y depletion in the case of coatings. However, several studies focusing on a range of compositions with a rare earth level below 1 at.% confirm the existence of the REE also for TiAl alloys upon addition of Y [23,24] and Hf [27].

This manuscript is part of our work on the development of ODS TiAl and its consolidation by spark plasma sintering (SPS), selective laser melting (SLM) and laser direct metal deposition (DMD). In a first paper, the microstructure and Y<sub>2</sub>O<sub>3</sub> particle stability after processing and thermal treatment were characterized [28]. In this work, the effect of Y<sub>2</sub>O<sub>3</sub> addition to spark plasma sintered (SPS) and direct metal deposited (DMD) TiAl alloys on the mechanical properties and oxidation resistance are described.

## **2 Experimental**

### **2.1 Material**

The studied materials are SPS Ti-45Al-3Nb (at.%), and SPS and direct metal deposited (DMD) Ti-45Al-3Nb+<0.2Y<sub>2</sub>O<sub>3</sub> (at.%, mol.%). Hereafter the two alloys are called OX 45-3 and OX 45-3 ODS. The bulk material is consolidated from mechanically alloyed powder supplied by MBN Nanomaterialia, Italy. After obtaining the non-ODS OX 45-3 alloy in a size fraction of 10 μm to 45 μm for SPS, Y<sub>2</sub>O<sub>3</sub> is added upon high energy ball milling to form the ODS variant. Powder fractions in the size ranges of 10–45 μm and 46–106 μm are retrieved for SPS and DMD consolidation, respectively. The details of consolidation have been described in [28]. In brief, SPS consolidation of cylindrical billets (d = 50 mm) is performed at 50 MPa and 1598 K with a dwell time of 2 min using a HP D 10 commercial setup (FCT Systeme GmbH, Germany). A combination of a tri-beam coaxial powder delivery head with a TruDisk 8002 laser source (Trumpf Laser GmbH, Germany) mounted on a Reis RV60-40 robot (Reis Robotics, Germany) is used for DMD. The material is deposited in a (15x70x15) mm<sup>3</sup> cuboid with a bidirectional strategy at a volume energy density of 120 J/mm<sup>3</sup>. All material is heat treated at 1123 K for 12 h in vacuum. Cast TNB-V5 (Ti-45Al-5Nb-0.2C-0.2B) supplied by the Helmholtz-Zentrum Geesthacht, Germany, was used as reference for oxidation testing.

### **2.2 Mechanical testing**

Mechanical testing in the range of 293 K to 1073 K was performed with a tensile/compression module developed by Kammrath & Weiss, Germany ( $F_{\max} = \pm 5$  kN). All room temperature tests were performed in air, while the experiments at elevated temperatures were conducted at  $2 \cdot 10^{-5}$  mbar in a vacuum setup. The specimen geometry is a flat dog bone shape with a nominal gauge length of 10 mm, a width of 3 mm and a thickness of 1 mm (Supplementary Figures S1 and S2). Prior to machining the bulk material was heat treated at 1123 K for 12 h in vacuum for stress relief. Specimens were produced from bulk material by electro-discharge machining (EDM) and ground to P600 using SiC grinding paper. Grinding was performed parallel to the testing direction to avoid stress concentration at surface flaws. Tests at room temperature are performed with an extensometer attached to the specimen (EXA10-1x, Sandner, Germany,  $\pm 0.1 \mu\text{m}$ ) while the load is measured by a load cell ( $\pm 0.5$  N). For tests at elevated temperature a ceramic heating element covered with a W plate was mounted directly to the specimen with W springs. Temperature was measured by a thermocouple in the W plate close to the specimens interface and actively controlled  $\pm 1$  K. Prior to testing the setup was heated with 40 K/min from room temperature to the test temperature to allow thermal equilibration of the specimen. The thermal expansion and developing compressive stress were compensated using the load control mode of the module maintaining an effective load of  $0 \pm 5$  N during heating. After reaching the target temperature and a dwell time of 2 min the specimen was loaded in tensile mode with 5 N/s until fracture. Due to geometric restrictions the extensometer could not be mounted for the high-temperature experiments. Consequently, only the machine elongation and load were measured for these experiments. We assume that the machine stiffness is, in good approximation, independent of the testing temperature (only the gauge length of the specimen is actively heated) and that the same specimen geometry is applied. Hence, the machine elongation  $e_m$  and specimen elongation  $e_s$  are correlated by

$$e_s = c(F) \cdot e_m \quad (1)$$

where  $c$  is a function of the applied load  $F$ , which was determined based on the room temperature experiments, where both  $e_m$  and  $e_s$  were simultaneously measured. This procedure allows the estimation of the fracture strain  $\varepsilon_f$  and yield stresses for different temperatures. As the  $\varepsilon_f$  of titanium aluminides is typically one order of magnitude lower than in conventional Ti alloys, the yield stress at 0.1% plastic strain,  $Rp_{0.1}$ , is used in this work.

### 2.3 Oxidation resistance

The degradation behavior of consolidated TiAl alloys was measured at 923 K and 1073 K in static laboratory air. The tests were performed in an air furnace equipped with  $\text{MoSi}_2$  heating elements (Nabertherm, Switzerland). The temperature was measured by a K-type thermocouple (Labfacility Ltd, UK,  $\pm 2.5$  K) placed directly beneath the alumina test containers. The setup consisted of an alumina

crucible (Almath Crucibles Ltd, UK) with the specimen suspended by Pt-Rh wire from an alumina bar (Supplementary Figure S3). This ensured access of air to all surfaces of the specimen while the specimen was irradiated only by the surrounding alumina crucible separating it from the hot heating filaments. The specimen geometry was a (10 x 10 x 1) mm<sup>3</sup> platelet, ground up to a P1200 SiC paper (15.3 μm average particle diameter) and cleaned in acetone in an ultrasonic bath. Prior to and after testing the specimen size was measured with calipers (Mitutoyo CD-15DC, ±0.01 mm) and the weight was determined on a precision balance (ALJ 120-4, Kern & Sohn, Germany, ±0.1 mg). Gaussian error propagation was applied to estimate the errors introduced by the uncertainties of specimen size and weight. These errors are later shown as error bars with the data points. In order to compare the observed oxide scale growth rates of the different studied alloys, a parabolic growth model according to

$$\left(\frac{\Delta m}{A}\right)^2 = k_p \cdot t \quad (2)$$

where  $t$  is the time,  $m$  is the mass,  $A$  is the surface area and  $k_p$  is the parabolic growth constant, was fitted to the data.

## 2.4 Characterization

Scanning electron microscopy (SEM) using a Philips XL30 ESEM, equipped with a secondary electron (SE) and a backscattered electron imaging (BSE) detector, was applied to the specimen fracture surfaces and oxide scales. Oxide cross-sections and energy dispersive X-ray (EDX) scans thereof for qualitative compositional analysis were prepared by focused ion beam milling (FIB) using a FEI Helios 660 G3 UC equipped with an Oxford Instruments X-Max 150 EDX detector and an in-column detector (ICD) providing compositional contrast. Electron transparent lamellae for transmission electron microscopy (TEM) investigations were prepared by FIB on a dual beam FEI Helios 600i using the lift out technique and a final polishing step at 2 kV was applied. The prepared lamellae were analyzed by scanning transmission electron microscopy (STEM) on an aberration-corrected JEOL 2100FCs S/TEM operating at 200 kV.

X-ray diffraction (XRD) measurements were performed using a Bruker D8 DISCOVER (Bruker, Germany) equipped with a LynxEye 1D detector. Measurements were performed with Cu K $\alpha$  radiation at 40 kV and 40 mA with a step size of 0.02° ± 0.0001° (2 $\theta$ ).

### 3 Results and discussion

#### 3.1 Alloy microstructure

Figure 1 shows the microstructure of the studied materials. SPS OX 45-3 has a near-lamellar structure with a large fraction of lamellar colonies of  $\gamma$ -TiAl and  $\alpha_2$ -Ti<sub>3</sub>Al phases,  $\gamma$ -phase located at the colony boundaries and residual porosity can be observed (Figure 1a). Upon addition of Y<sub>2</sub>O<sub>3</sub> in SPS OX 45-3 ODS the microstructure is refined yielding smaller colony sizes around 5  $\mu$ m to 10  $\mu$ m and an increased fraction of equiaxed  $\gamma$  phase as well as  $\alpha_2$  phase (Figure 1b). In DMD OX 45-3 ODS a fine structure consisting predominantly of lamellar colonies around 5 microns, coarsened oxide particles and residual pores are observed (Figure 1c).

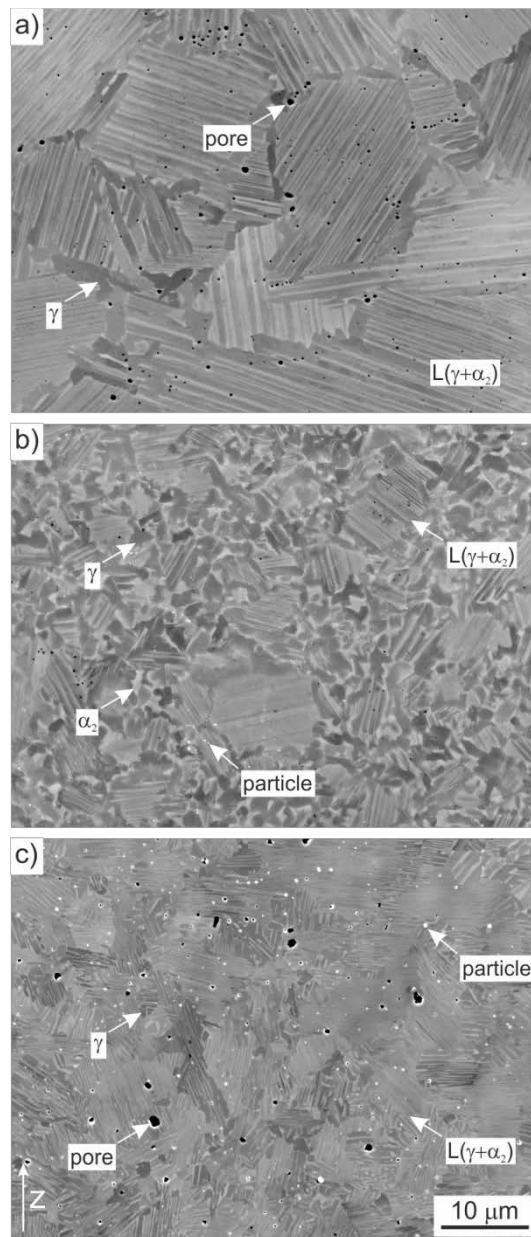


**Figure 1** Microstructures of a) SPS OX 45-3, b) SPS OX 45-3 ODS and c) DMD OX 45-3 ODS after heat treatment at 1123 K for 12h. Microstructural features as well as the build direction in DMD (z) are indicated. The scale bar in c) is valid for all micrographs.

### 3.1 Mechanical performance

The addition of ODS particles has a clear influence on the tensile properties of ternary Ti-45Al-3Nb at room temperature. Figure 2a shows the tensile stress-strain curves for SPS OX 45-3 and OX 45-3 ODS tested until fracture at room temperature. The ODS variant has a higher yield point  $R_{p0.1}$  of  $794 \pm 12$  MPa (+34 %) and higher ultimate strength  $R_m$  of  $856 \pm 0.1$  MPa (+14 %) but a lower total fracture strain  $\epsilon_f$  of  $0.76 \pm 0.04$  % (-17 %) compared to the ODS-free variant with  $593 \pm 10$  MPa,  $751 \pm 8$  MPa and  $0.91 \pm 0.03$  %, respectively. The Young's modulus of both variants is close to 170 GPa based on the linear elastic part of the stress-strain curve. Only small scatter is observed between the individual specimens, selected randomly from different regions in the consolidated billet. This indicates good microstructural homogeneity throughout the SPS consolidated material. The mechanical performance of SPS OX 45-3 ODS remains superior to the ODS-free variant up to 1073 K. Figure 2b shows the evolution of  $R_{p0.1}$ ,  $R_m$  and  $\epsilon_f$  for both variants after testing at 293 K, 873 K, 973 K and 1073 K. The  $R_{p0.1}$  of SPS OX 45-3 ODS is slightly reduced at 873 K compared to its maximum value at room temperature before increasing again at 973 K and 1073 K. The  $R_m$  shows a similar behavior with an initial decrease and later recovery. The very similar evolution of  $R_m$  and  $\epsilon_f$  indicates a critical strain based failure mechanism leading to premature fracture and lower  $R_m$  at intermediate temperatures. This is also evident from the increased standard deviation of  $R_m$  at 973 K, which is caused by a strong scattering of the obtained values for four specimens. This high standard deviation is unusual for this alloy comparing all the other data. Detailed analysis shows that the measured values of  $R_m$  at 973 K are 747 MPa, 755 MPa, 775 MPa and 856 MPa. At the same time the  $R_{p0.1}$  value shows only little scattering. The maximum strain at fracture is 0.77 % for 856 MPa while the minimum observed strain is 0.61 % for 755 MPa.

In the ODS-free variant SPS OX 45-3 the  $R_{p0.1}$  first increases at 873 K before it strongly decreases at 973 K and increases again at 1073 K. The  $R_m$  and  $\epsilon_f$  show a similar evolution which is inverse to the trends of the  $R_{p0.1}$ . First, both values decrease when tested up to 873 K. At 973 K the  $R_m$  recovers to  $734 \pm 22$  MPa while  $\epsilon_f$  reaches its maximum of  $1.08 \pm 0.14$  %. At 1073 K both values decrease again. The mechanical properties of DMD OX 45-3 at 293 K and 1073 K exceed the values of ODS-free SPS OX 45-3 but remain inferior to SPS OX 45-3 ODS (Figure 2b). All mechanical data is reported in Supplementary Table S1.

To understand the differences in mechanical performance and the cause of failure, the fracture surfaces are examined by SEM. Figure 3 shows the characteristic features observed in SPS OX 45-3 ODS after fracture at 293 K, 873 K, 973 K and 1073 K. The insets show the region of the crack origin as identified by the typical star-like crack pattern forming around it. Three main failure modes are observed: trans-lamellar (TL), inter-granular (IG) and "feathery" trans-lamellar (FTL) fracture. The trans-



lamellar modes are observed in the lamellar colonies of  $\alpha_2 + \gamma$ . The TL mode shows a ragged crack surface following the lamellar interfaces before crossing individual lamellae. The FTL mode crosses several lamellae without directional change along the interfaces. The IG mode is observed in the equiaxed region following the grain boundaries of the  $\gamma$  phase. It is evident from the micrographs that SPS OX 45-3 ODS shows a very similar fracture mode at all temperatures. The origin of the crack is related to a cleavage fracture of the intermetallic matrix. Based on the size of these cleaved regions it is believed that is related to the lamellar colonies in the material. No mass contrast between the crack origin and the surrounding matrix is observed, indicating intrinsic crack initiation in the microstructure. At room temperature a small inclusion is observed close to the cleaved region. Although probably responsible for initiation of final fracture its influence on the mechanical performance though appears to be minimal based on the superior strength of the material. Figure 4 shows the fracture surfaces of SPS OX 45-3 after testing at 293 K to 1073 K. The same three fracture modes as in the ODS-variant are observed, including the additional inter-lamellar (IL) mode. The IL mode is observed in the lamellar colonies and separates the individual lamellae, leading to large planar features. At 293 K the predominant fracture mode is the TL mode (Figure 4a). The IG and FTL modes are also observed in the  $\gamma$ -rich regions and across lamellae, respectively. At 873 K the FTL mode appears on larger areas while the equiaxed  $\gamma$  shows very distinct inter-granular fracture with no apparent ductility (Figure 4b). At 973 K the IL mode is observed, thereby completely changing the appearance of the fracture surfaces. At the same time the FTL mode vanishes (Figure 4c). The fracture surface at 1073 K is similar to the one observed at 973 K showing TL, IG and IL modes (Figure 4d). The inset shows also separation cracks forming in between the IG and IL zones in the equiaxed  $\gamma$  and lamellar colonies. The change in fracture mode between 873 K and 973 K is accompanied with a strong increase in ductility and reduced yield strength (Figure 2b). This indicates that the IL mode is actually a ductile fracture mode compared to the brittle IG and TL modes. The replacement of the FTL mode by the IL mode could indicate that the FTL mode is also a ductile fracture mode. However, based on the macroscopic ductility this cannot be confirmed due to its limited occurrence within the fracture surface.

Also the ODS-variant shows an increased ductility at high temperature with abundance of the FTL mode (Figure 3d). This indicates that indeed the FTL mode is a sign of ductility in the lamellar colonies and can explain the increased strain at fracture. Furthermore, the IL and FTL modes appear to be strongly related with the direction of the crack growth changing from trans-lamellar at low temperature to inter-lamellar in the IL mode at high temperature in the ODS-free variant while the predominant direction remains trans-lamellar in the ODS-variant. Consequently, the IL mode is not observed in this sample.

Figure 5 shows the fracture surfaces of DMD OX 45-3 ODS tested at 293 K and 1073 K. At both temperatures the origin of fracture is a pore close to the specimen surface with a diameter of around

100  $\mu\text{m}$  (Figure 5a and c). This explains the lower  $R_m$  and  $\varepsilon_f$  observed in DMD material compared to its SPS counterpart. Due to stress concentration and a reduction of the load bearing area, the DMD specimens fail at lower macroscopic stresses and strains. A close examination of the fracture surface reveals a similar fracture surface as in SPS material (Figure 5b and d). At room temperature fracture occurs predominantly with the TL and IG modes with little occurrence of the FTL mode. At 1073 K all three fracture modes persist with increased fraction of the FTL mode. This indicates a similar deformation and fracture mechanism for the OX 45-3 ODS material processed by SPS or DMD.

The significant increase in yield point of the ODS-variant can be attributed to the addition of dispersoids. However, the underlying mechanism for the higher yield point is not only depending on the presence of the dispersoids and their interaction with dislocations. A second and very important contribution is from the microstructure itself: the ODS-variant has a fine microstructure with equiaxed  $\gamma$  phase between small lamellar colonies forming a duplex to near-lamellar alloy. The ODS-free alloy has less  $\gamma$  surrounding larger lamellar colonies and is thus closer to a near-lamellar alloy. It is well known that in TiAl alloys all constituents, equiaxed  $\gamma$ , lamellar colonies and the lamellar structure itself follow a Hall-Petch relationship with increased strength with reduced feature size [29]. Duplex microstructures combining lamellar colonies and a significant fraction of equiaxed  $\gamma$  have typically already high strength, but are inferior to near-lamellar microstructures providing the highest strength in TiAl alloys [30]. Taking into account these findings, the microstructure of the ODS-free variant should actually provide the higher strength than the structure richer in equiaxed  $\gamma$  found in the ODS-variant based on its general microstructure. A refinement effect upon ODS addition of each microstructural feature can however lead to significantly enhanced strength as the Hall-Petch constants of TiAl alloys for lamellar microstructures have been found to be unusually high up to  $5 \text{ MPa}\cdot\text{m}^{1/2}$  compared to common metals with values close or below unity [29]. Separation of the individual effects, however, remains difficult as microstructure, properties and alloy composition are intertwined in TiAl alloys. At elevated temperature the abnormal mechanical behavior of the intermetallic phases contributes to the strength retention. The single-crystalline  $\gamma$  and  $\alpha_2$  show an abnormal strength increase with increasing temperature with their maximum yield stress around 873 K and 1173 K, respectively [31]. In technical alloys this leads to a ductile-to-brittle transition around 923 K to 1073 K, as  $\gamma$  starts to soften. This is in agreement with the observations in the ODS-free OX 45-3 alloy. The addition of dispersoids suppresses the softening reaction found in OX 45-3 which is a clear benefit for the ODS variant providing stable yield stress for all tested temperatures. The softening is explained by increased mobility of previously dissociated and locked super-dislocations recombining due to thermal activation [31]. While the dissociating contribution disappears, the dispersoids remain stable and continue to hinder dislocation movement. Consequently, superior yield stress is maintained to higher temperature in ODS TiAl alloys.

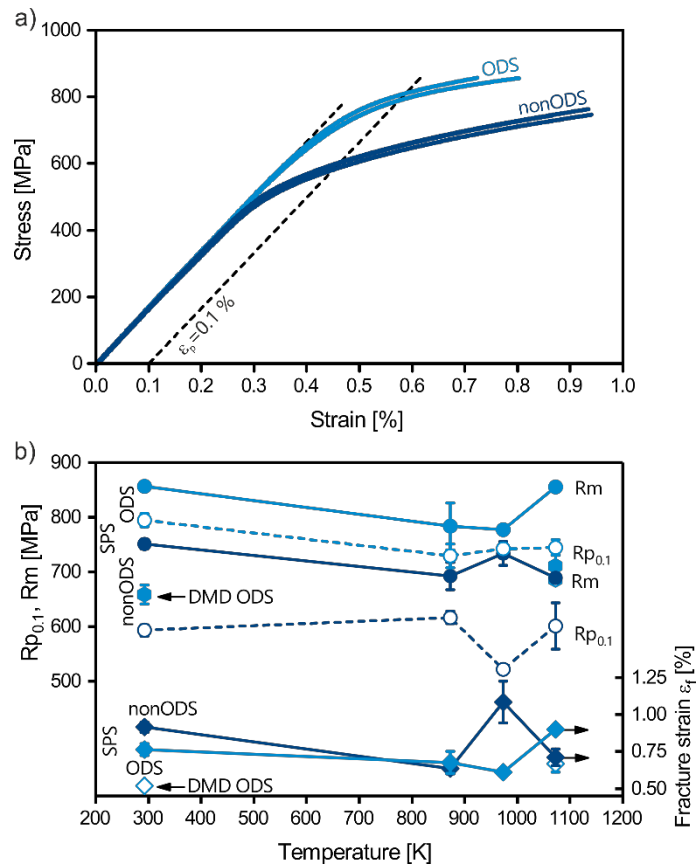


**Figure 2** a) Tensile stress-strain curves for SPS OX 45-3 (nonODS, n=3) and OX 45-3 ODS (ODS, n=2) at room temperature. b) Mechanical performance of non-ODS OX 45-3 and SPS and DMD OX 45-3 ODS from 293 K to 1073 K. DMD data is shown as hexagons for  $R_m$  and  $R_{p0.1}$  and open diamonds for  $\epsilon_f$ .

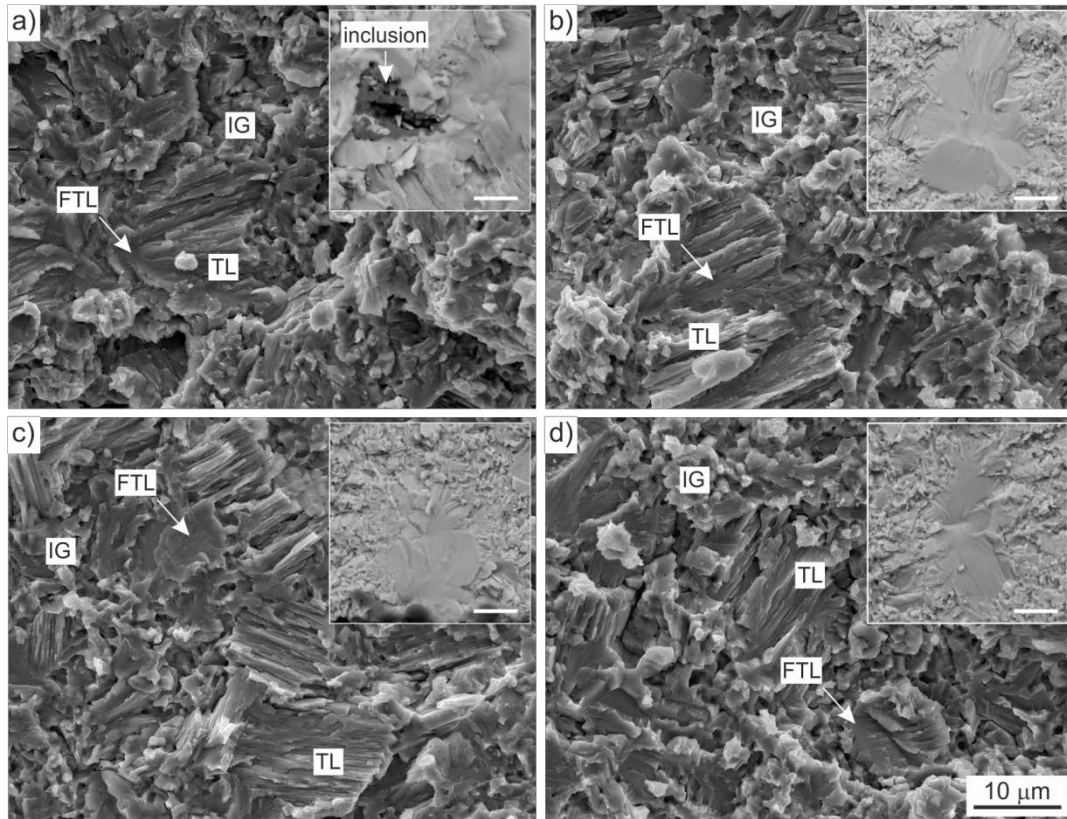


**Figure 3** SE SEM micrographs of the fracture surface of OX 45-3 ODS tensile tested at a) 293 K, b) 873 K, c) 973 K and d) 1073 K. Insets: BSE SEM micrographs of the origin of fracture. The characteristic fracture modes trans-lamellar (TL), feathery trans-lamellar (FTL) and inter-granular (IG) are indicated. The scale bar in d) applies for a-d). Insets: scale bar = 10  $\mu\text{m}$ .

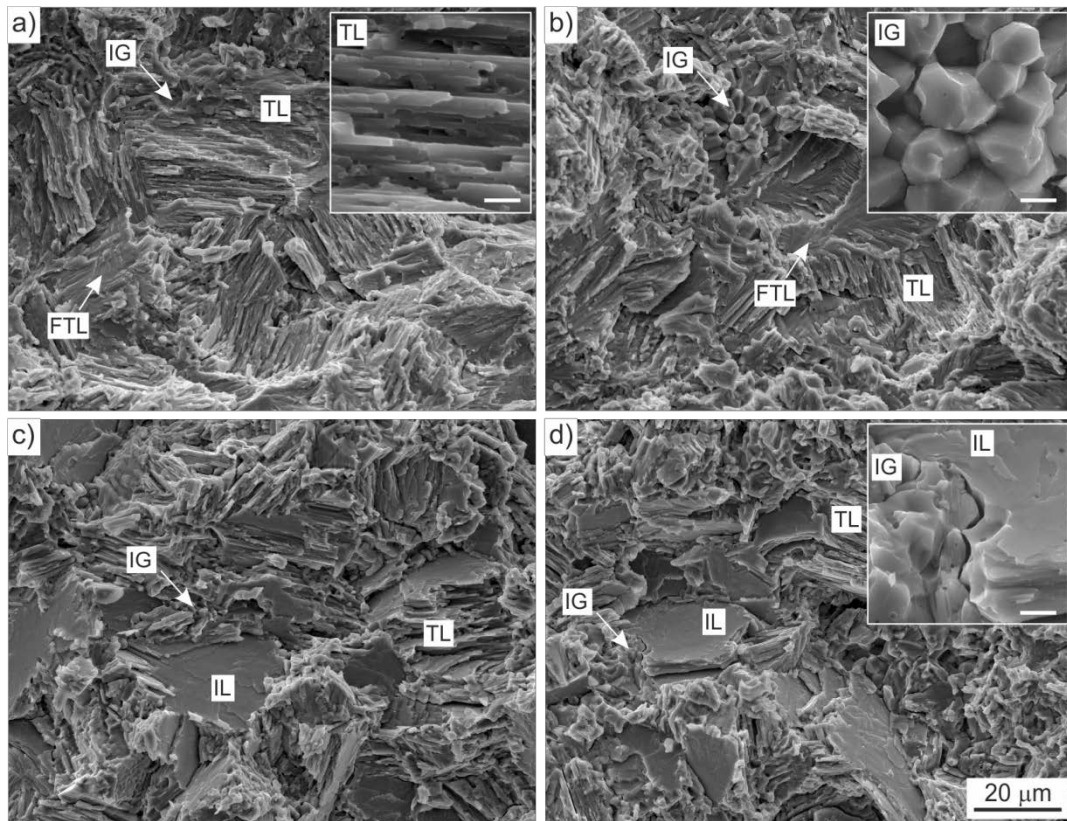


**Figure 4** SE SEM micrographs (SE contrast/image) of the fracture surface of OX 45-3 tensile tested at a) 293 K, b) 873 K, c) 973 K and d) 1073 K. The characteristic fracture modes TL, FTL, inter-lamellar (IL) and IG are indicated. The scale bar in d) applies for a-d). Inset a): scale bar = 1  $\mu\text{m}$ , insets b, d): scale bar = 2  $\mu\text{m}$ .

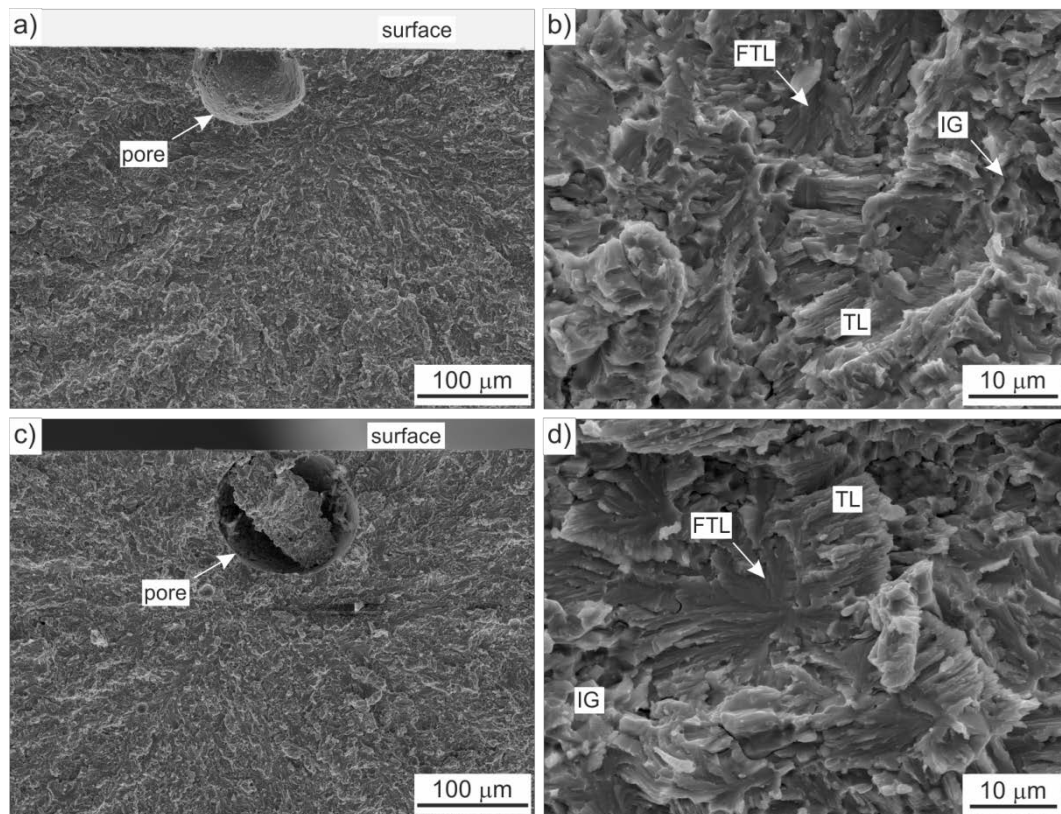


**Figure 5** SE SEM micrographs (SE contrast/image) of the fracture surface of DMD OX 45-3 ODS tensile tested at a, b) 293 K and c, d) 1073 K. The characteristic fracture modes TL, FTL and IG are indicated.

### 3.2 Oxidation resistance

#### Weight gain

Figure 6 shows the weight gain per unit area for ODS-free SPS OX 45-3, SPS and DMD OX 45-3 ODS and TNB-V5. Comparing the ODS-free and ODS-containing variant processed by SPS a reduced weight gain is clearly observed upon addition of the  $Y_2O_3$ . SPS OX 45-3 ODS shows a parabolic growth of the oxide scale up to the maximum tested time of 924 h. At this point spallation is observed at the edges of the specimens. Over the complete duration of the oxidation test, the parabolic growth mode is maintained which is also seen by the data points lying on a line with a slope of 0.5 on a logarithmic scale (inset Figure 6). The ODS-free OX 45-3 alloy shows initially parabolic growth up to 360 h. For longer test duration accelerated growth is observed which is also evident from an increased slope on the logarithmic scale. Consequently, no fitted parabolic growth model is shown for OX 45-3. However, the data up to 360 h follows a parabolic model and is thus included in Table 1 for comparison. The fitted  $k_p$  value for the OX 45-3 ODS variant is about half the value of the ODS-free alloy with  $1.9 \cdot 10^{-10} \text{ kg}^2 \text{ m}^{-4} \text{ s}^{-1}$  and  $3.7 \cdot 10^{-10} \text{ kg}^2 \text{ m}^{-4} \text{ s}^{-1}$ , respectively. For DMD processed OX 45-3 ODS another reduction is observed to  $0.9 \cdot 10^{-10} \text{ kg}^2 \text{ m}^{-4} \text{ s}^{-1}$ . It is hypothesized that this is an effect of compositional homogenization during DMD as well as potential doping effects by Y due to particle dissolution.

Comparing the oxidation resistance of OX 45-3 ODS to TNB-V5, the SPS material is slightly inferior and the DMD material is superior. The reference alloy TNB-V5 is also a Ti-Al-Nb based alloy with additions

of B and C, containing an increased amount of Nb compared to OX 45-3 (ODS). Upon the addition of the elements Nb, C, and B, to TiAl alloys increased oxidation resistance has been observed [18]. In the case of Ti-Al-Nb alloys additions exceeding 5 at.% Nb have been found to have significantly increased oxidation resistance [19]. The difference in composition thus explains the increased oxidation resistance of TNB-V5 compared to OX 45-3. It is an important observation that the addition of <0.2 mol.% Y<sub>2</sub>O<sub>3</sub> leads to a similar oxidation resistance to an increased Nb alloying level by 2 at.% plus the addition of C and B. The  $k_p$  value for TNB-V5 determined in this work for a test duration of 1001 h is increased by  $0.3 \cdot 10^{-10} \text{ kg}^2 \cdot \text{m}^{-4} \cdot \text{s}^{-1}$  compared to the value reported by Masset and Schütze for 62 h [32] (Table 1). However, the weight gain at 24 h of TNB-V5 observed in this work is overestimated by the fit over the complete test duration (see inset Figure 6). Consequently, a lower  $k_p$  is determined for short-term testing and explains the slight difference between reported values and the ones obtained in this work.

**Table 1** Parabolic growth rates  $k_p$  for OX 45-3, OX 45-3 ODS and TNB-V5 at 1073 K.

Alloy	$k_p \cdot 10^{-10} \text{ (kg}^2 \cdot \text{m}^{-4} \cdot \text{s}^{-1}\text{)}$	Evaluated time t (h)	Reference
SPS OX 45-3	3.7	0 < t < 360	This work
SPS OX 45-3 ODS	1.9	0 < t < 924	This work
DMD OX 45-3 ODS	0.9	0 < t < 1000	This work
TNB-V5	1.4	0 < t < 1001	This work
	1.1	0 < t < 62	[32]

### Morphology and phase evolution of the formed oxide scale

The evolution of the morphology of the oxide scale on OX 45-3 ODS at 1073 K initially shows the formation of a fine grained, Al<sub>2</sub>O<sub>3</sub>-rich scale after 10 h (Figure 7a). Some coarsened oxides appear, being TiO<sub>2</sub> based on their composition. According to XRD, the scale after 10 h consists of TiO<sub>2</sub> (rutile) and  $\alpha$ -Al<sub>2</sub>O<sub>3</sub> (corundum) and trace amounts of TiN and Ti<sub>2</sub>AlN (Figure 8). After 100 h exposure the TiO<sub>2</sub> covers most of the surface with only a few spots left where the fine grained Al<sub>2</sub>O<sub>3</sub>-layer remains visible (Figure 7b). This is also represented by a strong increase in TiO<sub>2</sub> peak intensities in XRD. The reflections of the TiN-phase decrease in intensity, indicating its formation in the initial stages of oxidation and its location close to the alloy-scale interface. After 354 h of oxidation the scale surface shows mainly coarse, faceted TiO<sub>2</sub> crystals with a lateral size below 5  $\mu\text{m}$  (Figure 7c). Upon exposure for 924 h no significant changes of the oxide scale surface morphology are observed (Figure 7d). The scale

continues to increase in thickness and mass, as it is evident from Figure 6 but also from vanishing substrate and TiN signal intensities in XRD (Figure 8).

In order to elucidate the effect of the  $Y_2O_3$  addition in OX 45-3 ODS, the morphology evolution of the ODS-free variant OX 45-3 and TNB-V5 is studied. OX 45-3 shows accelerated degradation compared to the ODS-variant. After 24 h exposure of OX 45-3 at 1073 K the surface is already covered by  $TiO_2$  (Figure 9a). XRD also indicates the presence of  $\alpha-Al_2O_3$  as well as traces of TiN and  $Ti_2AlN$  (Figure 10a). Upon 1001 h of exposure, the surface structure is coarsened with large  $TiO_2$ -crystals forming with lateral sizes exceeding 10  $\mu m$  (Figure 9c). XRD indicates fast and predominant formation of  $TiO_2$ . The scale formed on the reference alloy TNB-V5 after 1001 h at 1073 K consists out of coarse, faceted  $TiO_2$  as well as fine-grained regions in between them (Figure 9d). Comparing the morphologies of the formed scale after similar exposure time on OX 45-3, OX 45-3 ODS and TNB-V5 shows a very similar behavior of the latter two. Both form a scale with a bimodal grain size distribution of coarser  $TiO_2$  and finer  $TiO_2 + Al_2O_3$  in between. This similarity also observed in the XRD spectra after the maximum test time (Figure 10b). While the spectra for OX 45-3 ODS and TNB-V5 are virtually the same, showing the presence of a significant fraction of  $Al_2O_3$  beside the major  $TiO_2$ , the spectrum of OX 45-3 is dominated by the presence of  $TiO_2$ . Beside this difference, the general phase evolution appears to be similar for all alloys.

Figure 11 shows a comparison of FIB cross-section across the oxide scale in OX 45-3, OX 45-3 ODS and TNB-V5 after exposure at 1073 K. As indicated by the weight gain, OX 45-3 forms a thicker scale compared to OX 45-3 ODS and TNB-V5 (Figure 11a-c). Despite the change in thickness, the micrographs show a similar multiphase, layered and complex scale structure. As evident from the XRD measurements, the outermost region consists of a coarse  $TiO_2$  layer. EDX line-scans across the scale confirm a region consisting of fine grained  $Al_2O_3 + TiO_2$  below the surface layer (Figure 12). Towards the base material, the  $Al_2O_3$  phase disappears leaving behind a region of predominantly  $TiO_2$  phase. At the alloy-scale interface bulky  $Al_2O_3$ -rich phases are observed together with a thin layer enriched in Ti, Al and N as well as Nb-rich phases (Figure 11d-f). Below the alloy-scale interface, Ti-depletion is observed in the base material. Simultaneously, Nb is enriched in this region with its maximum concentration directly below the oxide scale. Nb is also incorporated into the first  $TiO_2$ -rich zone, but is absent in the outer  $Al_2O_3 + TiO_2$  and surface  $TiO_2$ -layer. OX 45-3 shows internal degradation with the formation of N-rich phases and small Al-oxides along grain boundaries (Figure 11d). Consistently, EDX shows signal variations for N and O in the subsurface zone (Figure 12a). The internal degradation is clearly attenuated in OX 45-3 ODS with much less penetration depth into the subsurface zone (Figure 10e). TNB-V5 shows no internal degradation (Figure 11f).

The general behavior of the three studied alloys is schematically summarized in Figure 13. In the initial state, the alloy has a thin native oxide layer due to the high affinity of Ti and Al to oxidize. After



exposure to air (<24 h at 1073 K), the surface is covered with fine grained  $\text{Al}_2\text{O}_3$  and TiN as well as dispersed coarser  $\text{TiO}_2$  crystals. Upon prolonged exposure to air,  $\text{TiO}_2$  starts to overgrow the fine grained  $\text{Al}_2\text{O}_3$ -rich layer as  $\text{TiO}_2$  provides a fast diffusion path for oxygen. Additionally, N diffuses towards the alloy, forming various nitride phases. Ti and Al diffuse into the scale and form new oxides, which leads to a multiphase structure. Nb as a slowly diffusing element enriches at the lower interface, forming Nb-rich phases. After long term exposure of 1000 h the final layered oxide structure is formed with  $\text{TiO}_2$  as the outermost layer. The underlying fine grained  $\text{Al}_2\text{O}_3$ -rich layer controls the diffusion of oxygen and thus scale growth. Toward the alloy-scale interface a mixed layer of Ti- and Al-oxides is formed. The interface itself consists of a mixture of nitrides, Al-oxides, and Nb-rich phases. Enhanced diffusion of N along grain boundaries favors the formation of nitrides in the sub-scale zone. Due to selective oxidation of Ti and Al these elements are depleted leaving behind a Nb-enriched zone with typically higher  $\alpha_2$  content due to compositional shifts towards higher Ti content.

While all three alloys show a similar scale evolution in terms of the sequence of the formed phases, their weight gains have been found to be very different, where the ODS-containing variant and the Nb-richer TNB-V5 show similarly low growth kinetics. In the past the beneficial effect of Nb and the similar elements Mo and W have been attributed to the stabilization of  $\text{Al}_2\text{O}_3$  forming in a sub-surface barrier layer as well as in the inner  $\text{TiO}_2$ -rich region [18]. Consequently, inward transport of oxygen along the  $\text{TiO}_2$  is strongly reduced and higher oxidation resistance is achieved. Similar effects on the stability of  $\text{Al}_2\text{O}_3$  have been described for Y-doped TiAl alloys [24]. Comparing the results for OX 45-3 and OX 45-3 ODS, this effect is also triggered by additions of  $\text{Y}_2\text{O}_3$  in the form of finely distributed dispersoids (Fig. 11e). Unlike in elemental addition, the Y is concentrated in the stable dispersoids avoiding detrimental effects as formation of large internal  $\text{Y}_2\text{O}_3$ -particles, as observed by Haanappel et al. [25]. This effect is not observed in this work by the addition of Y in the form of a stable dispersion of Y-based oxides.

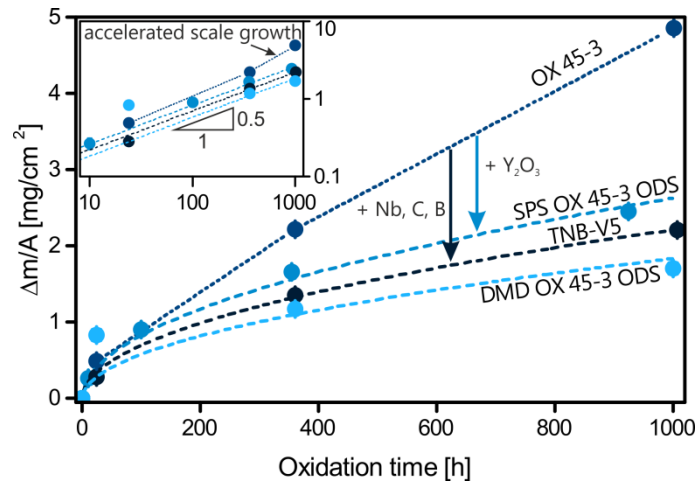


**Figure 6** Weight gain of OX 45-3, SPS and DMD OX 45-3 ODS and TNB-V5 at 1073 K in static laboratory air. For OX 45-3 ODS and TNB-V5 fitted parabolic curves are shown (- -). The data points for OX 45-3 have been connected to guide the reader's eye (·-·).

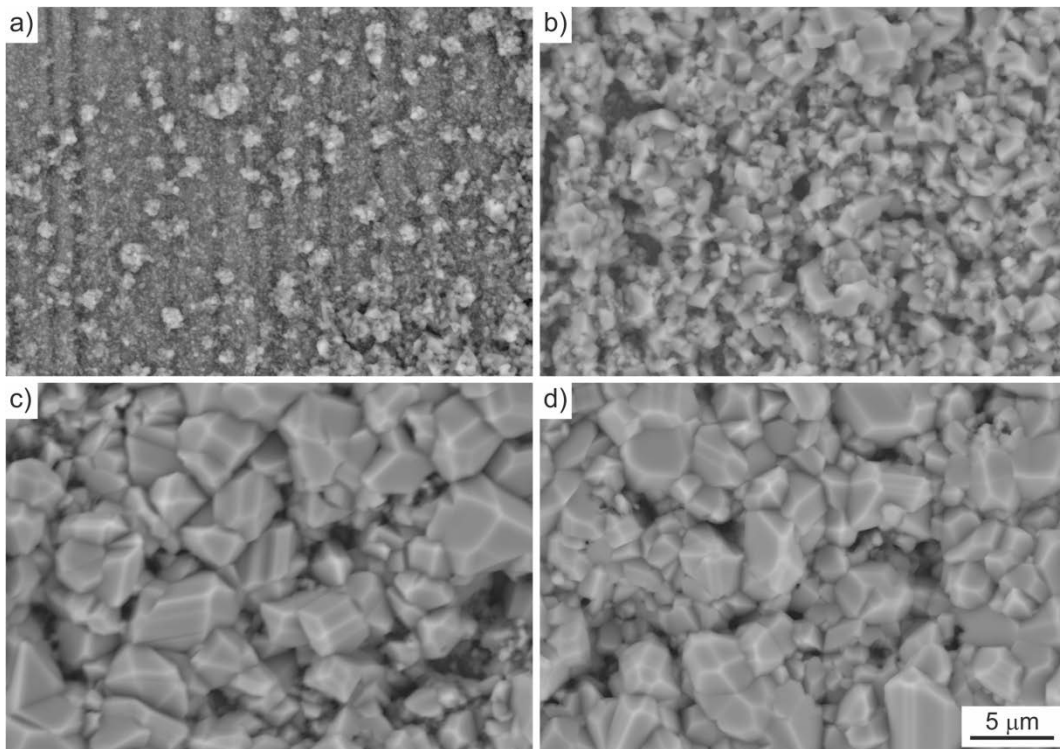


**Figure 7** BSE SEM top-view micrographs of OX 45-3 ODS after a) 10 h, b) 100 h, c) 354 h and d) 924 h at 1073 K in air. The scale bar in d) is valid for a-d).

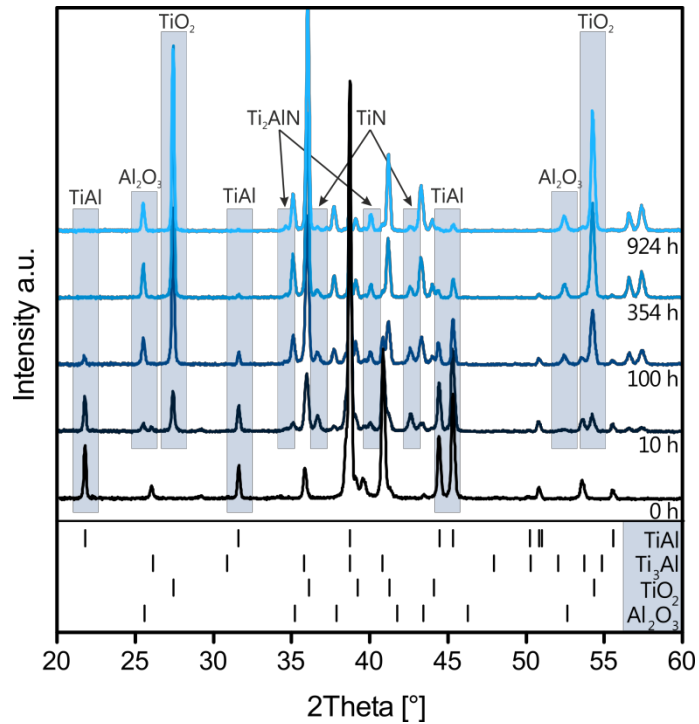


**Figure 8** XRD spectra of oxidized OX 45-3 ODS at 1073 K. The peak positions of the major phases  $\gamma$  TiAl,  $\alpha_2$  Ti<sub>3</sub>Al, TiO<sub>2</sub> (rutile) and  $\alpha$ -Al<sub>2</sub>O<sub>3</sub> (corundum) are indicated as well as the evolution of their prominent peaks. Traces of TiN and Ti<sub>2</sub>AlN peaks are marked with arrows (↓).

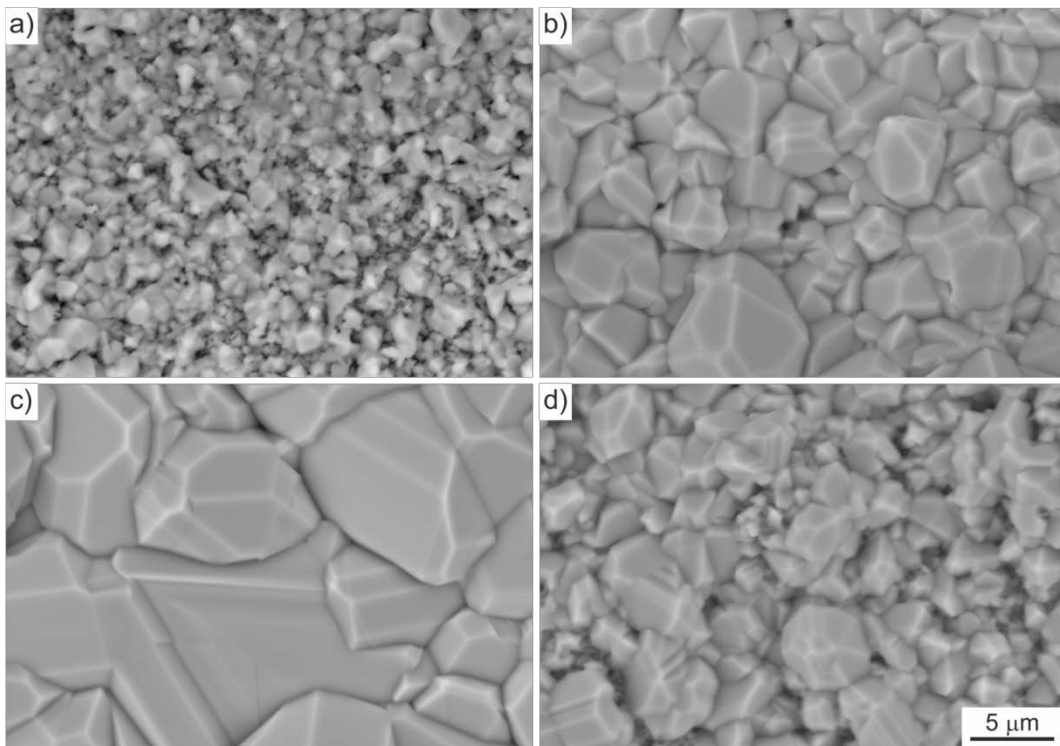


**Figure 9** BSE SEM top-view micrographs of a-c) OX 45-3 and d) TNB-V5 after a) 24 h, b) 360 h, and c, d) 1001 h at 1073 K in air. The scale bar in d) is valid for a-d).

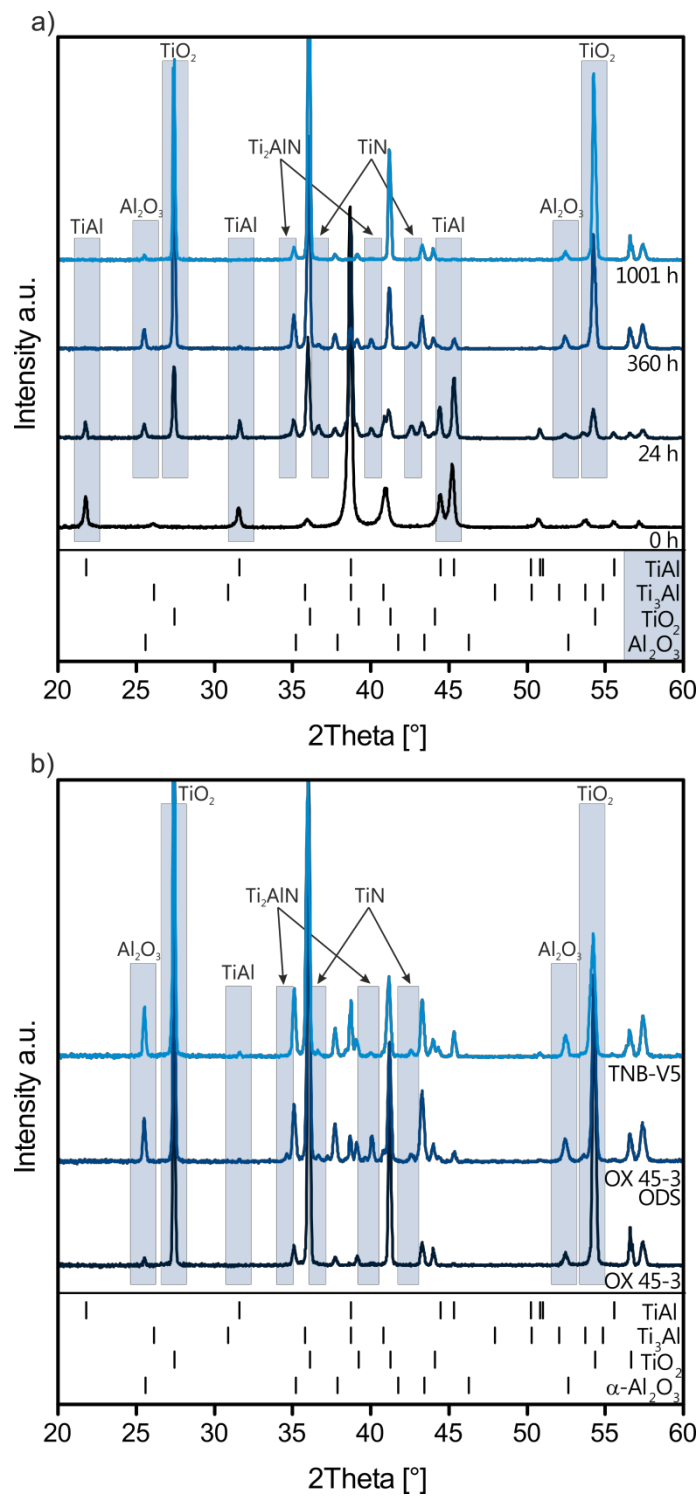


**Figure 10** XRD spectra of a) oxidized OX 45-3 at 1073 K and b) OX 45-3 (bottom), OX 45-3 ODS (center) and TNB-V5 (top) oxidized at 1073 K for 1001 h, 924 h and 1001 h, respectively.

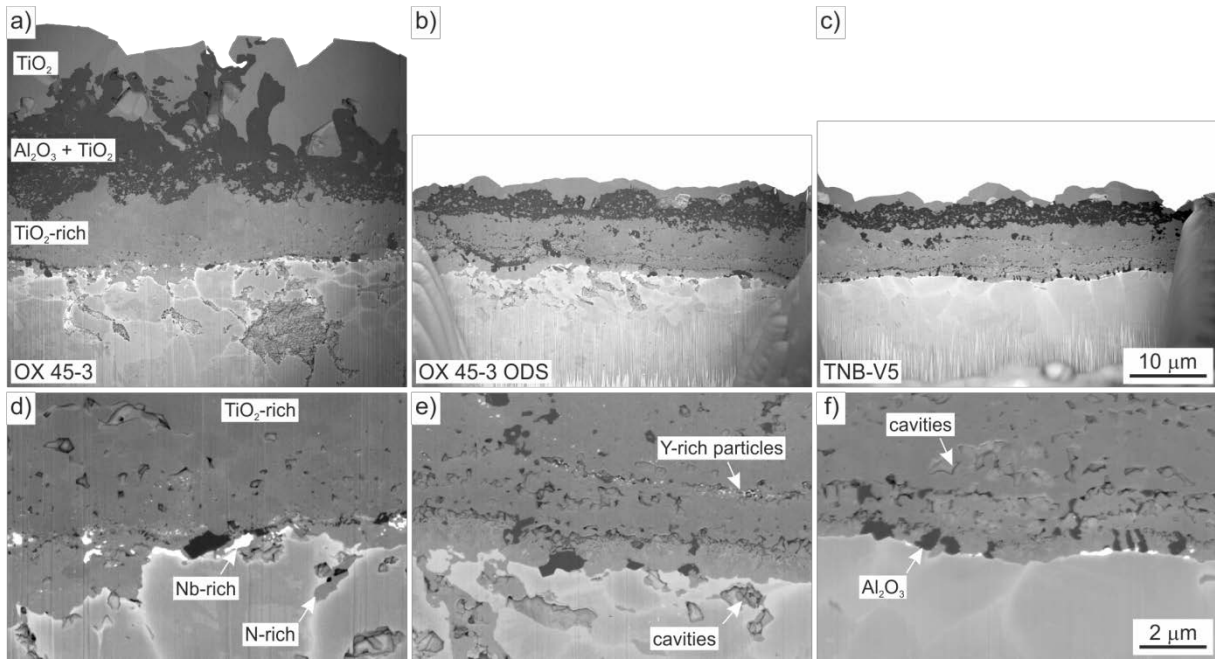


**Figure 11** FIB ICD SEM (Z-contrast) cross-sections of OX 45-3 (a, d) after 1001 h, OX 45-3 (b, e) ODS after 924 h and TNB-V5 after 1001 h exposure to air at 1073 K (c, f). The scale bar in c) is valid for a-c), the scale bar in f) for d-f).

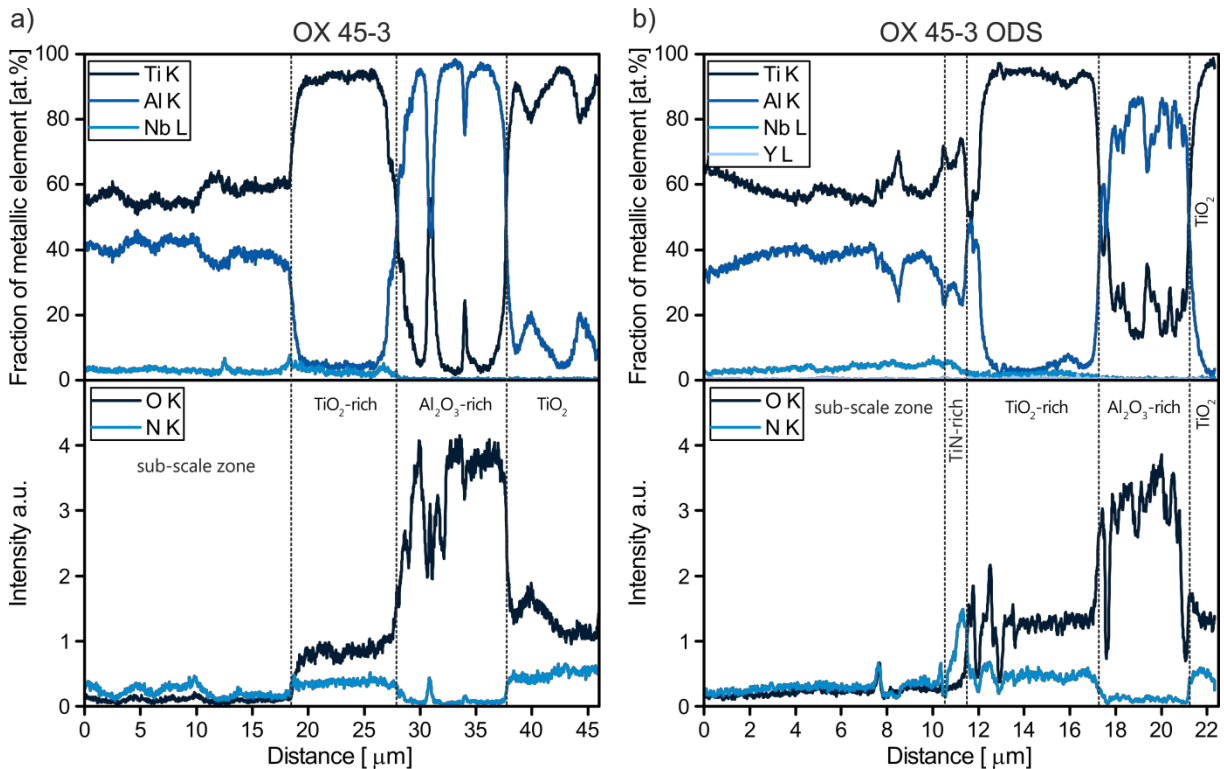


**Figure 12** EDX line scans across the formed oxide scales in a) OX 45-3 after 1001 h and b) OX 45-3 ODS after 924 h exposure to air at 1073 K showing the atomic percentage of the main metallic elements (top) and the intensity of the light elements O and N (bottom).

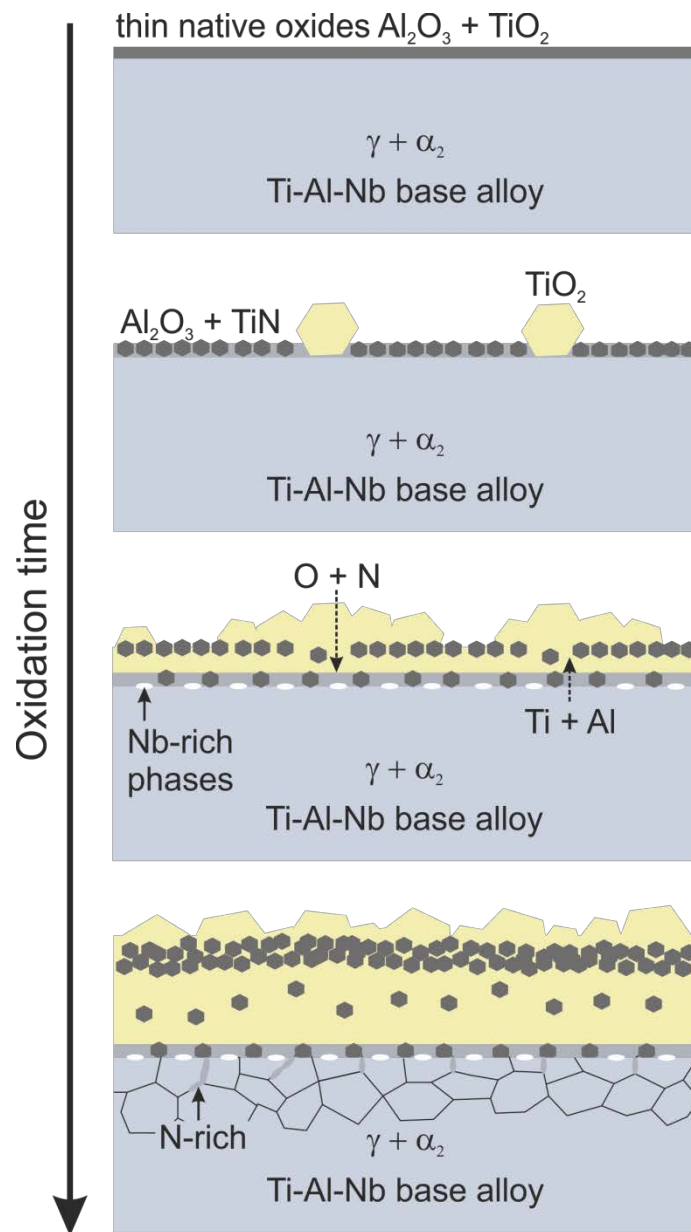


**Figure 13** General oxidation processes and structural evolution upon oxidation of the studied Ti-Al-Nb base alloys at 1073 K. a) native state, b) short term exposure up to 24 h, c) intermediate stage (24 h < t < 1000 h), d) final state after 1000 h.

### Size evolution of the dispersoids at high temperature

The stability of the dispersoids and their size evolution is determined for the OX 45-3 ODS variant after exposure to air at 923 K and 1073 K after 987 h and 924 h, respectively (Figure 14). After testing at both temperatures, the dispersoids remain stable and well distributed throughout the intermetallic matrix (Figures 14a and 14c). The particles are observed in the equiaxed region consisting of  $\gamma$  and  $\alpha_2$  as well as in the lamellar  $\alpha_2 + \gamma$  colonies, where no preference for either phase is found. The dispersoids are globular and partly faceted, with diameters between sub-10 nm up to 150 nm. In both conditions a multitude of dispersoids is found on phase or grain boundaries, indicating a strong pinning effect by the dispersoids and consequently reduced grain growth due to their presence in the ODS-variant

(Figures 14b and 14d). Coarser dispersoids exert a high enough pinning force, which leads to locally curved grain boundaries. This clearly indicates the beneficial effects of a portion of larger particles on the microstructure stability at high temperatures. A similar effect has also been observed at short term annealing at high temperatures in OX 45-3 ODS [28]. Upon exposure to air at 923 K and 1073 K the dispersoids show little change in their size distribution. Figure 15 shows the size distributions after both exposure conditions as well as the initial state in the stabilized OX 45-3 ODS alloy. After consolidation by SPS, the following stress relief and microstructural stabilization annealing at 1123 K for 12 h, the resulting mean dispersoid diameter is 29 nm. The log-normal shape of the distribution indicates the highest fraction of particles at a slightly smaller diameter of around 23 nm. The number density of particles is  $4.4 \cdot 10^{20} \text{ m}^{-3}$ . Upon exposure at 923 K for 987 h the resulting size distribution is shifted to 26 nm with its maximum relative frequency in the size class of 15 to 20 nm with a particle number density of  $5.3 \cdot 10^{20} \text{ m}^{-3}$ . A similar oxidation time at 1073 K leads to a slight particle coarsening, shifting the size distribution to a median of 32 nm at a particle number density of  $4.4 \cdot 10^{20} \text{ m}^{-3}$ . While the relative frequency of the fine dispersoids is reduced, a larger amount of coarser ones appears simultaneously indicating continued growth of particles of all sizes. The appearance of a high fraction of dispersoids with sub-median size after oxidation at 923 K could be attributed to fast coarsening of very fine precipitates or re-precipitation from the matrix. In the present case the latter appears to be the case, as the fraction of small dispersoids after consolidation appears not to be high enough to explain such behavior. The increased number density also suggests the formation of new particles. But it has also to be noted that the measurement of particles below 5 nm is difficult based on their low contrast to the surrounding matrix. The re-precipitation mechanism can be understood taking into account the production route of the alloy. Upon high-energy ball milling the added  $\text{Y}_2\text{O}_3$  is finely dispersed and potentially partially dissolved into the matrix alloy. After precipitation and growth upon SPS consolidation and annealing, the formed particles are in a metastable equilibrium with the matrix, based on the relative stabilities of the phases involved. It was shown in the past that even in equilibrium a portion of the initially added dispersoid material remains in solution [4]. This leads to a doping of the TiAl alloy matrix with Y and O in the case of  $\text{Y}_2\text{O}_3$  addition. Upon long-term oxidation at moderate temperature, the formation of new particles appears to be faster than the growth of the existing ones, leading to an effective shift of the total size distribution towards smaller diameters. At higher temperature this effect is not observed. Additional effects may be chemistry changes of the particles formed. Changing from a Y-rich to a Y-lean phase, new particles can be formed by incorporation of the abundant Ti and Al as well as O. To unambiguously determine such an effect a large amount of measurements on the formed particles is needed to ensure statistical meaning which is not the goal of the presented study. However, this remains an important topic for future studies of this class of intermetallics. Apart from the discussion about the underlying cause of the observed shifts

in the particle size distribution by a few nanometers, it can be clearly stated that the particles in OX 45-3 ODS exhibit a low coarsening tendency and are stable at 1073 K for 1000 h.

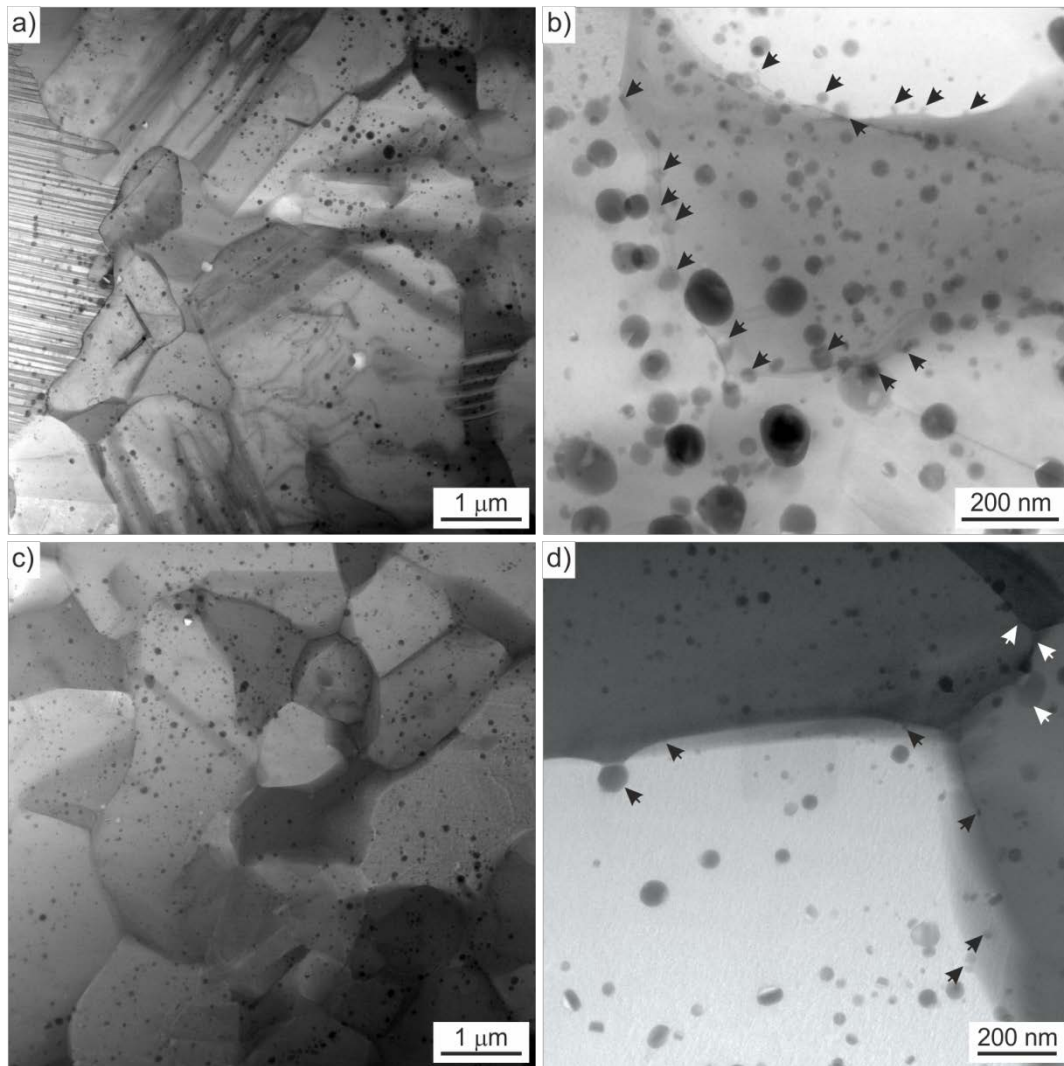


**Figure 14** Bright-field STEM micrographs of the microstructure of SPS OX 45-3 ODS after a, b) 987 h at 923 K and c, d) 924 h at 1073 K in static laboratory air. Boundary pinning is indicated with arrows.



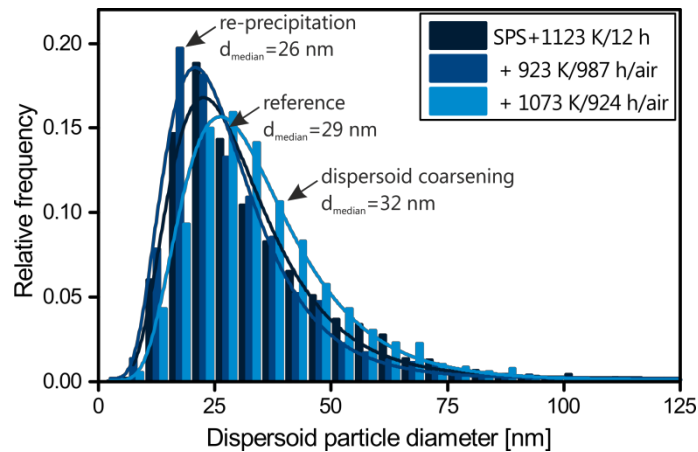


**Figure 15** Size distribution of ODS particles in solid state SPS sintered and stabilized material after exposure for 987 h at 923 K and 924 h at 1073 K. Least-square-fitted log-normal distribution curves are shown overlaid.

#### 4 Summary and conclusion

- At room temperature, SPS OX 45-3 ODS has a 34% higher yield point, 14% higher ultimate tensile strength at a reduction in fracture strain of 17% compared to SPS OX 45-3. The ODS variant retains its superior yield point and ultimate strength up to 1073 K.
- The ultimate strength of DMD specimens is limited by the presence of pores leading to premature fracture.
- The fracture surfaces of OX 45-3 show increased tendency for interlamellar failure at high temperatures. SPS and DMD OX 45-3 ODS shows similar fracture surfaces from 293 K to 1073 K with preferred trans-lamellar fracture.
- The addition of  $Y_2O_3$  increases the oxidation resistance of mechanically alloyed and SPS sintered Ti-45Al-3Nb at 1073 K by a factor of two compared to the ODS-free variant. DMD material is superior to SPS material.
- Upon oxidation a complex oxide scale is formed. XRD shows the presence of  $TiO_2$ ,  $Al_2O_3$  and TiN and  $Ti_2AlN$  nitride phases, where  $TiO_2$  forms the outermost layer. All alloys form protective  $Al_2O_3$  as part of their oxide scales.
- The Y-based dispersoids remain stable at 923 K and 1073 K up to 1000 h with minimal changes in median size from 29 nm in the initial state to 26 nm at 923 K and 32 nm at 1073 K, respectively. Increased number densities from  $4.4$  to  $5.3 \cdot 10^{20} \text{ m}^{-3}$  indicate precipitation of new particles at 923 K.

The achieved oxidation behavior is comparable to a commercial TNB-V5 alloy richer in Nb and additionally alloyed with C and B. The addition of  $<0.2 \text{ mol.}\% Y_2O_3$  provides similar resistance as the

effects of additional 2 at.% Nb and 0.2 at.% C and B. The addition of dispersed  $Y_2O_3$  opens a new possibility to further enhance the oxidation resistance of TiAl alloys alloyed already to their maximum allowable contents of Nb or other elements as W and Mo based on the desired set of phases. Based on the presented results, the addition of ODS particles is considered a promising way to further enhance the properties of TiAl alloys. In the future, detailed creep studies are needed to explore the limits of the ODS approach in TiAl material.

### Acknowledgement

The research leading to these results has received funding from the European Union Seventh Framework Program [FP7/2007-2013] under grant agreement no. 310279 (OXIGEN).

### References

- [1] F.H. Froes, C. Suryanarayana, D. Eliezer, Synthesis, properties and applications of titanium aluminides, *J. Mater. Sci.* 27 (1992) 5113–5140. doi:10.1007/BF00553381.
- [2] K.S. Kumar, G. Bao, Intermetallic-matrix composites: An Overview, *Compos. Sci. Technol.* 52 (1994) 127–150.
- [3] A.V. Antonova, K.B. Povarova, A.A. Drozdov, Composite materials with an intermetallic matrix based on nickel and titanium monoaluminides hardened by oxide particles or fibers, *Russ. Metall. Met.* 2011 (2012) 853–864. doi:10.1134/S0036029511090023.
- [4] M. Grujicic, S. Arokiaraj, Chemical compatibility between zirconia dispersion and gamma titanium aluminide matrix, *Calphad.* 17 (1993) 133–140. doi:10.1016/0364-5916(93)90013-2.
- [5] C.C. Koch, Intermetallic matrix composites prepared by mechanical alloying—a review, *Mater. Sci. Eng. A.* 244 (1998) 39–48.
- [6] O.A. Skachkov, K.B. Povarova, A.A. Drozdov, A.E. Morozov, S.V. Pozharov, Deformation and Heat Treatment of NiAl-Y<sub>2</sub>O<sub>3</sub>-Based Powder Alloys: I. Deformation and Production of Various Pressed Sections, *Russ. Metall.* 3 (2013) 217–219.
- [7] S.L. Kampe, J.D. Bryant, L. Christodoulou, Creep Deformation of TiB<sub>2</sub>-Reinforced Near- $\gamma$  Titanium Aluminides, *Metall. Trans. A.* 22 (1991) 447–454.
- [8] F.H. Froes, Titanium Aluminides: Science, Technology, Applications and Synthesis by Mechanical Alloying, *J. Mater. Chem. Sci. Technol.* 10 (1994) 251–262.
- [9] W. Liu, J.N. Dupont, Fabrication of Carbide-Particle-Reinforced Titanium Aluminide-Matrix Composites by Laser-Engineered Net Shaping, *Metall. Mater. Trans. A.* 35 (2004) 1133–1140.
- [10] Schwartz, D.S., P. Fraundorf, S.M.L. Sastry, TEM study of B- and Er-containing dispersoids in rapidly solidified dispersion-strengthened titanium aluminide alloys, *Ultramicroscopy.* 37 (1991) 310–317.
- [11] C. Suryanarayana, F.H. Froes, Mechanical Alloying of Titanium-Base Alloys, *Adv. Mater.* 5 (1993) 96–106.
- [12] P.B. Trivedi, E.G. Baburaj, A. Genc, L. Ovecoglu, S.N. Patankar, F.H. Froes, Grain-size control in Ti-48Al-2Cr-2Nb with yttrium additions, *Metall. Mater. Trans. A.* 33A (2002) 2729–2736.
- [13] Z.W. Li, W. Gao, D.L. Zhang, Z.H. Cai, High temperature oxidation behaviour of a TiAl–Al<sub>2</sub>O<sub>3</sub> intermetallic matrix composite, *Corros. Sci.* 46 (2004) 1997–2007. doi:10.1016/j.corros.2003.10.026.
- [14] K. Zhang, W. Fen, J. Zhu, H. Wu, Mechanical Properties and Microstructure of Al<sub>2</sub>O<sub>3</sub>/TiAl in Situ Composites Doped with Cr and V<sub>2</sub>O<sub>5</sub>, *Sci. Sinter.* 44 (2012) 73–80.

- [15] D.P. Whittle, J. Stringer, Improvements in High Temperature Oxidation Resistance by Additions of Reactive Elements or Oxide Dispersions, *Philos. Trans. R. Soc. Lond. Math. Phys. Eng. Sci.* 295 (1980) 309–329. doi:10.1098/rsta.1980.0124.
- [16] J. Stringer, Proceedings of the 2nd International symposium on High Temperature Corrosion of Advanced Materials and Coatings The reactive element effect in high-temperature corrosion, *Mater. Sci. Eng. A.* 120 (1989) 129–137. doi:10.1016/0921-5093(89)90730-2.
- [17] B.A. Pint, Progress in understanding the reactive element effect since the Whittle and Stringer literature review, in: *Proc John Stringer Symp. High Temp. Corros.*, ASM International, 2003: pp. 9–19.
- [18] Y. Shida, H. Anada, The effect of various ternary additives on the oxidation behavior of TiAl in high-temperature air, *Oxid. Met.* 45 (1996) 197–219.
- [19] J.W. Fergus, Review of the effect of alloy composition on the growth rates of scales formed during oxidation of gamma titanium aluminide alloys, *Mater. Sci. Eng. A.* 338 (2002) 108–125. doi:10.1016/S0921-5093(02)00064-3.
- [20] W. Zhang, G. Chen, Z. Sun, Oxidation of ternary Ti–18Nb–48Al and Ti–10Nb–45Al alloys, *Scr. Metall. Mater.* 28 (1993) 563–567. doi:10.1016/0956-716X(93)90197-Z.
- [21] A. Gil, B. Rajchel, N. Zheng, W.J. Quadackers, H. Nickel, The influence of implanted chromium and yttrium on the oxidation behaviour of TiAl-based intermetallics, *J. Mater. Sci.* 30 (1995) 5793–5798. doi:10.1007/BF00356723.
- [22] J.P. Kim, H.G. Jung, K.Y. Kim, Al+Y codeposition using EB-PVD method for improvement of high-temperature oxidation resistance of TiAl, *Surf. Coat. Technol.* 112 (1999) 91–97. doi:10.1016/S0257-8972(98)00787-7.
- [23] K. Kasahara, Y. Ikeda, T. Kimura, T. Tsujimoto, Effects of additions of Y and rare-earth metals on the cyclic oxidation of TiAl alloys, *J. Jpn. Inst. Met.* (1996) 907–913.
- [24] Y. Wu, S.K. Hwang, Microstructural refinement and improvement of mechanical properties and oxidation resistance in EPM TiAl-based intermetallics with yttrium addition, *Acta Mater.* 50 (2002) 1479–1493. doi:10.1016/S1359-6454(02)00006-X.
- [25] V.A.C. Haanappel, H. Clemens, M.F. Stroosnijder, The high temperature oxidation behaviour of high and low alloyed TiAl-based intermetallics, *Intermetallics.* 10 (2002) 293–305.
- [26] M.K. Lei, X.P. Zhu, X.J. Wang, Oxidation Resistance of Ion-Implanted  $\gamma$ -TiAl-Base Intermetallics, *Oxid. Met.* 58 (2002) 361–374. doi:10.1023/A:1020162922745.
- [27] S. Taniguchi, T. Shibata, Influence of additional elements on the oxidation behaviour of TiAl, *Intermetallics.* 4 (1996) 85–S93. doi:10.1016/0966-9795(96)00017-9.
- [28] C. Kenel, K. Dawson, C. Hauser, J. Barras, G. Dasargyri, T. Bauer, A. Colella, A.B. Spierings, G.J. Tatlock, C. Leinenbach, K. Wegener, Microstructure and oxide particle stability in a novel ODS  $\gamma$ -TiAl alloy processed by spark plasma sintering and laser additive manufacturing submitted, 2017.
- [29] D.M. Dimiduk, P.M. Hazzledine, T.A. Parthasarathy, M.G. Mendiratta, S. Seshagiri, The role of grain size and selected microstructural parameters in strengthening fully lamellar TiAl alloys, *Metall. Mater. Trans. A.* 29 (1998) 37–47. doi:10.1007/s11661-998-0157-3.
- [30] Y.-W. Kim, Ordered intermetallic alloys, Part III: Gamma titanium aluminides, *JOM.* 46 (1994) 30–39.
- [31] S. Djanarthany, J.-C. Viala, J. Bouix, An overview of monolithic titanium aluminides based on Ti3Al and TiAl, *Mater. Chem. Phys.* 72 (2001) 301–319.
- [32] P.J. Masset, M. Schütze, Oxidation Tests with Untreated and F-Treated TNBV5 Alloys, *ECS Trans.* 25 (2010) 45–56. doi:10.1149/1.3315795.

Supplementary

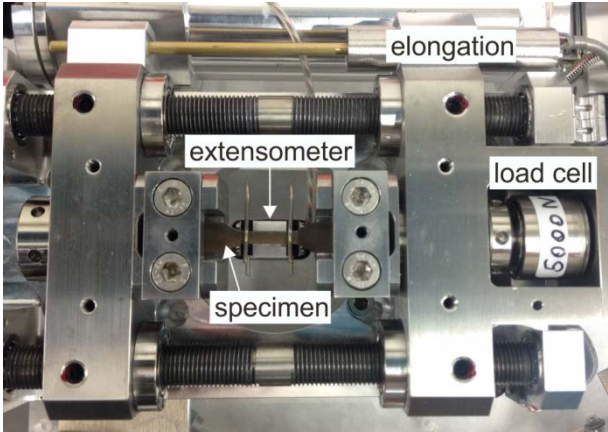


Figure S 1 Test setup for mechanical testing of small dog bone specimens.

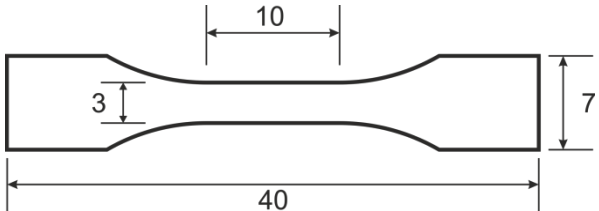


Figure S 2 Specimen geometry for mechanical testing.

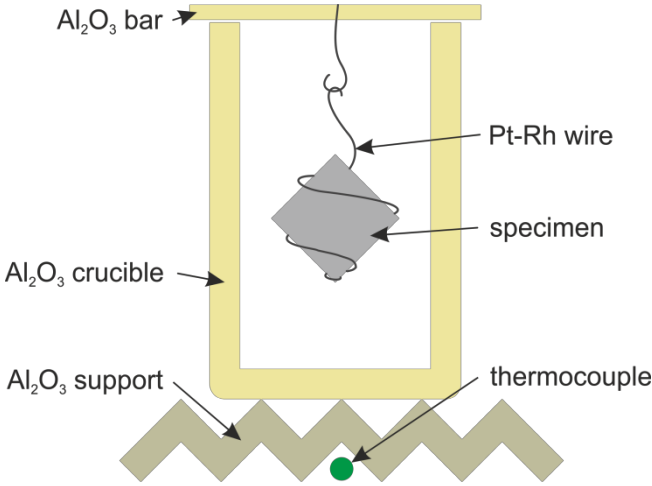


Figure S 3 Test setup for oxidation testing in air at 1073 K. The complete assembly is placed in a furnace.

**Table S 1** Static mechanical properties of SPS OX 45-3 and SPS and DMD OX 45-3 ODS. (-) no Rp0.1 obtained.

<b>Material</b>	<b>Temperature</b>	<b>Rp<sub>0.1</sub>±σ (MPa)</b>	<b>Rm±σ (MPa)</b>	<b>ε<sub>f</sub>±σ (%)</b>
SPS OX 45-3	293	794±12	856±0.1	0.76±0.04
	873	729±22	783±43	0.68±0.07
	973	742±6	777±0.4	0.61±0.02
	1073	745±14	855±3	0.90±0.01
SPS OX 45-3 ODS	293	593±10	751±8	0.91±0.03
	873	617±11	692±25	0.64±0.04
	973	521±8	734±22	1.08±0.14
	1073	601±42	689±9	0.71±0.06
DMD OX 45-3 ODS	293	-	659±18	0.52±0.02
	1073	686±5	711±21	0.67±0.06